BIOCHEMISTRY
including biophysical chemistry & molecular biology
Article

Biochemistry **2010,** *49,* 5799–5809 5799
DOI: 10.1021/bi100721b

Kinetics of ATP and TNP-ATP Binding to the Active Site of CheA from *Thermotoga maritima*[†]

Anna K. Eaton and Richard C. Stewart*

Department of Cell Biology and Molecular Genetics, University of Maryland, College Park, Maryland 20742

Received May 6, 2010; Revised Manuscript Received June 10, 2010

ABSTRACT: The mechanism of nucleotide binding to the active site of *Thermotoga maritima* CheA was investigated using stopped-flow fluorescence experiments that monitored binding of ATP and TNP-ATP to the catalytic domain (P4) of CheA that had been engineered to include a tryptophan residue as a fluorescent reporter group at the active site ($P4^{F487W}$). Rapid decreases in protein intrinsic fluorescence and increases in TNP-ATP fluorescence were observed during binding reactions, and time courses were analyzed to define the kinetic mechanisms for ATP and TNP-ATP binding. This analysis indicated that binding of ATP(Mg^{2+}) to $P4^{F487W}$ involves a single reversible step with a k_{on} of $0.92 \pm 0.09\ \mu M^{-1}\ s^{-1}$, a k_{off} of $1.9 \pm 0.4\ s^{-1}$, and a K_d of 1.5−2.1 μM (all values determined at 4 °C). Binding of TNP-ATP(Mg^{2+}) to $P4^{F487W}$ involves a more complicated mechanism, requiring at least three sequential steps. Computer simulations and nonlinear regression analysis were used to estimate the rate constants of the forward and reverse reactions for each of the three steps in the reaction scheme

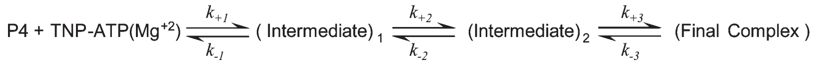

Similar analysis indicated that an alternative reaction scheme, involving a rate-limiting conformational change in P4 prior to TNP-ATP binding, did an equally good job of accounting for all of the kinetics results:

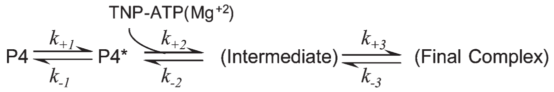

In both models, steps 2 and 3 have slow reversal rates that contribute to the high affinity of the active site for TNP-ATP (K_d = 0.015 μM). These results highlight the dramatic effect of the TNP moieties on CheA−nucleotide interactions, and they provide the first detailed information about the kinetic mechanism underlying interaction of a protein histidine kinase with this tight-binding inhibitor.

Signal transduction in prokaryotes often involves protein histidine kinases (PHKs)[1] that convey information from receptors to downstream signal transduction components (response regulators) via phosphorylation (*1*, *2*). Each PHK−RR pair constitutes a two-component signal transduction (TCST) pathway. For example, in the chemotaxis systems of *Escherichia coli* (*3*, *4*), *Thermotoga maritima* (*5*), and numerous other bacteria (*6*), CheA functions as a signal transducing PHK, directing the activities of RR proteins CheY and CheB via phosphorylation. Unlike other types of protein kinases, CheA and other signal transducing PHKs achieve phosphorylation of their target proteins via a mechanism that involves an obligatory autophosphorylation step: CheA binds ATP(Mg^{2+}) and catalyzes transfer of the γ-phosphoryl group from the nucleotide to a specific histidine side chain (H45) (*7*). This phosphohistidine then serves as a phospho-donating substrate for CheY and CheB, which are themselves enzymes that catalyze their own phosphorylation when they encounter phospho-CheA (*8*, *9*). Phosphorylated CheY interacts with the flagellar motor to promote changes in swimming direction (*10*, *11*), and phosphorylation of CheB regulates its participation in the chemotaxis sensory adaptation pathway (by activating its receptor-specific methylesterase activity) (*12*). The autokinase activity of CheA is regulated by cell surface receptor proteins that bind a variety of chemicals (*13*, *14*). This regulation allows bacteria to control their swimming movements in response to chemical gradients so that they can accomplish chemotaxis (*15*).

Here we describe our investigation of the kinetics of ATP binding by *T. maritima* CheA (Tm CheA), a protein that has been subjected to detailed structural and biochemical analysis (*16*−*21*). Tm CheA has a modular architecture in which five distinct structural domains make different contributions to the overall activities of the protein, and it is likely that CheA proteins in most other bacteria have structural and functional organizations that are very similar to this (*22*, *23*). ATP binding takes place in domain P4, and

---

[†] This research was supported by National Institutes of Health Grant GM052853 to R.C.S.

*To whom correspondence should be addressed. Phone: (301) 405-5475. Fax: (301) 314-9489. E-mail: alec@umd.edu.

[1] Abbreviations: DoF, degrees of freedom (number of independent observations, e.g., number of data points in all of the averaged stopped-flow time courses used for global analysis); F_{410}, fluorescence emission signal (at wavelengths of > 540 nm) when $\lambda_{excitation} = 410$ nm; F_{280}, fluorescence emission signal (at wavelengths of > 335 nm) when $\lambda_{excitation} = 280$ nm; MFC, molecular fluorescence coefficient; PHK, protein histidine kinase; RR, response regulator protein; TCST, two-component signal transduction; TNP-ATP, 2′(3′)-*O*-(2,4,6-trinitrophenyl)adenosine 5′-triphosphate; $\lambda_{excitation}$, excitation wavelength; σ_{DATA}, standard deviation of data (calculated using replicate time courses); σ_{FIT}, standard deviation of fit (calculated using residuals reflecting differences between simulated and observed signal intensities); χ^2, sum of the squared values of residuals (sum-squared error or SSE).

crystal structures of the P4·ATP(Mg^{2+}) and P4·TNP-ATP complexes are available (*17*). The CheA autophosphorylation site (H45) is located in domain P1. Domain P3 mediates dimer formation, while domain P5 is responsible for binding and regulatory interactions with CheW and chemotaxis receptor proteins. In a CheA dimer, there are two ATP binding sites and two phosphorylation sites (*18*). In previous work, we observed that the two active sites of the Tm CheA dimer are linked by strong negative cooperativity (*24*). This had the potential to greatly complicate analysis of the ATP binding kinetics. Therefore, for the kinetic analysis described here, we decided to limit our investigations to the active site located in an isolated P4 domain. Thus, all of the work described here involves a protein module with a single ATP binding site, and the protein–nucleotide complex has no ability to turn over since it lacks the domain that would provide the phospho-accepting histidine.

There are several compelling reasons for trying to understand, in detail, how the active sites of PHKs function. First, for numerous TCST pathways, regulation of the PHK active site is the key regulatory event that enables microbial cells to mount appropriate responses to stimuli, so understanding this active site is important for understanding how microbes perceive and respond to their worlds (*25*). Second, some PHKs in pathogenic microorganisms are essential for viability, while others regulate expression of virulence factors. Designing PHK-specific inhibitors could provide new antimicrobial drugs (*26*, *27*). In this regard, understanding how PHKs bind ATP at their active sites could be useful for designing such drugs. Fluorescent TNP-modified nucleotides may provide an informative starting point for understanding PHK active sites and how to inhibit them. TNP-ATP, for example, binds to CheA (*17*, *28*) and EnvZ (*29*) and with affinities that are much tighter than those observed with ATP. What accounts for this enhanced affinity? In the crystal structure of the *T. maritima* P4·TNP-ATP complex, the TNP group occupies a hydrophobic pocket adjacent to the ATP binding site, so favorable protein–TNP contacts in this pocket can contribute to the binding affinity (*17*). We investigated the kinetic mechanism underlying this tight binding of TNP-ATP to *T. maritima* CheA, and we compared this to the mechanism utilized by CheA for binding of unmodified ATP. Our findings indicate that the binding mechanisms are quite different, and they provide some insight into the kinetic basis underlying tight binding of TNP-ATP.

EXPERIMENTAL PROCEDURES

Chemicals and Reagents. 2′(3′)-*O*-(2,4,6-Trinitrophenyl)-adenosine 5′-triphosphate (TNP-ATP) was purchased from Invitrogen/Molecular Probes, Inc. [type T-7602, trisodium salt, supplied as a 5 mg/mL solution in 0.1 M Tris (pH 9)], and was stored in the dark at −20 °C. According to the supplier, this material had a purity of 96% (assessed by high-pressure liquid chromatography). We used thin layer chromatography as described by Grubmeyer and Penefsky (*30*) to check the purity of this material. Our analysis showed a single spot with the expected mobility. This approach could detect impurities comprising >3–5% of the material analyzed, so our results confirmed a purity of >95%. ATP was purchased from Roche Diagnostics, and ultrapure glycerol was from MP Biomedicals. All other chemicals were reagent grade and were purchased from Sigma or Fisher. Spectrophotometer readings in a Cary 50 instrument were used to determine nucleotide concentrations for solutions of TNP-ATP ($\varepsilon_{408} = 26.4\ mM^{-1}\ cm^{-1}$) (*31*) and for ATP solutions ($\varepsilon_{260} = 15.4\ mM^{-1}\ cm^{-1}$). TEG buffer (used for protein purification and storage) contained 0.5 mM Na_2EDTA, 10% (v/v) glycerol, and 50 mM Tris adjusted to pH 7.5 using hydrochloric acid. TnM buffer (used for binding titrations and binding kinetics experiments) contained 0.5 mM Na_2EDTA, 10% (v/v) glycerol, 25 mM NaCl, 50 mM potassium glutamate, 20 mM $MgCl_2$, and 25 mM Tris adjusted to pH 7.5.

Protein Expression and Purification. An expression plasmid for the *T. maritima* P4 domain (residues 356–540) was created by cloning a corresponding PCR fragment, flanked by *Nde*I and *Hin*dIII restriction sites, into pET28a (Novagen). This plasmid was used as the template for site-directed mutagenesis to change *cheA* codon 487 from TTC (Phe) to TGG (Trp) using the GeneTailor system and custom-synthesized oligonucleotides (Invitrogen). The resulting expression plasmid was used to overproduce His_6-tagged $P4^{F487W}$ in *E. coli* cells (BL21λDE3 from Invitrogen), and the protein was purified and stored as described previously (*24*). The concentration of this protein was determined spectrophotometrically using a calculated extinction coefficient ($5.5\ mM^{-1}\ cm^{-1}$) (*32*) that we confirmed using the Bio-Rad protein assay. We did not remove the His_6 tag from the $P4F^{487W}$ protein. To simplify the text, the presence of the His tag is not indicated explicitly in the remainder of this paper.

Fluorescence-Monitored TNP-ATP Binding Titrations. Binding site titrations were conducted as described previously (*24*) using samples (in TnM buffer) placed in 1 cm × 1 cm quartz fluorescence cuvettes, stirred continuously using a magnetic stir bar, and maintained at 4 °C using a Peltier thermal regulator attached to the cuvette holder. Fluorescence emission spectra were recorded and averaged using a PTI QuantaMaster instrument measuring counts per second (cps) in digital mode; excitation and emission slits were set to 2 nm. To monitor protein intrinsic fluorescence, $\lambda_{excitation}$ was set to 280 nm and emission spectra were recorded from 300 to 450 nm. To monitor TNP-ATP fluorescence, $\lambda_{excitation}$ was set to 410 nm and emission spectra were recorded from 450 to 650 nm. Each of the titrations depicted in the figures represents the average of at least two independent experiments conducted on different days using independently prepared protein and ligand solutions. Integrated fluorescence intensities were analyzed as described previously (*24*).

Rapid Reaction Measurements. Stopped-flow fluorescence experiments were performed using a KinTek SF2004 instrument that had a dead time of 2.5 ms, measured using the Massey procedure (*33*) under the same buffer and temperature conditions utilized for all of our experiments. The excitation wavelength (280, 410, or 520 nm) was set using a monochromator (excitation slits set to give a bandpass of 5 nm), and the emitted light was monitored with a photomultiplier after passing through a long-pass filter (WG335 or OG540). All data were collected using a single photomultiplier voltage setting so that signal intensities could be compared directly and used for global analysis. For single-mix experiments, each shot involved 1:1 mixing of 40 μL aliquots of protein and ligand and then collection of 1000 logarithmically arrayed data points over the next second (or 50 s for dissociation experiments). After collection of 10–15 such shots at a single nucleotide concentration, the time courses were averaged to generate a single composite time course of 1000 time points. Prior to analysis, each averaged time course was adjusted to account for the instrument dead time by addition of 2.5 ms to the poststop time points recorded by the instrument operating system. Each time-adjusted time course was further adjusted by subtraction of the fluorescence intensity of free TNP-ATP (determined in a separate experiment) and by correction for inner filter effects arising from the light absorbance properties of TNP-ATP. This inner filter correction involved multiplying the observed fluorescence signal by a correction factor [determined empirically, but corresponding to $10^{0.5\times A_{410}}$ (*34*), where A_{410} is the absorbance at 410 nm for a TNP-ATP solution in the flow chamber of the stopped-flow instrument]. This correction factor was applied to all of the experiments utilizing TNP-ATP and ranged from 1.0 at low TNP-ATP concentrations to 5.225 at 100 μM TNP-ATP. For double-mixing stopped-flow experiments, 40 μL samples of P4^{F487W} and TNP-ATP were mixed 1:1, allowed to "age" for a specified interval (6−250 ms), and then mixed with a 40 μL solution containing a high concentration of ATP(Mg^{2+}) before being introduced into the observation chamber.

Analysis of Rapid Reaction Data. Initial analysis of reaction time courses (adjusted as described above) was performed by conventional nonlinear regression analysis using SigmaPlot. For ATP binding experiments, time courses were fit well as single-exponential decays (Figure S1 of the Supporting Information); the k_{observed} values reported in the inset of Figure 2A were determined using this approach. For TNP-ATP experiments, time courses were all biphasic (with two well-resolved phases), and we followed the convention of fitting them as the sum of two exponential phases to generate estimates of the rate constants for the two phases (*35*). For example, the observed k_{fast} and k_{slow} values reported in Figure 5 were determined using this type of analysis. This initial analysis (conventional analysis) indicated the minimal number of steps in the overall reaction pathway and provided initial estimates of the rate constants for these steps. This information was then used as a starting point for more extensive global analysis using KinTek Global Kinetic Explorer (*36*, *37*). This program can quickly simulate time courses for any user-defined model (reaction scheme), and this ability is exploited by the DataFit function of the program to conduct "numerical integration" (automated, iterative, trial-and-error simulations) to find the optimal set of rate constants, i.e., the combination of rate constants that maximizes the fit of a data set (minimizing χ^2). This enabled automated optimization of fits to a data set that included three different types of experiments: binding kinetics, single-mix dissociation kinetics, and double-mixing dissociation experiments. In addition, an error analysis component of this program (FitSpace) was used to quantify the "goodness of fit" and to define upper and lower limits for each kinetic parameter (rate constants and molecular fluorescence coefficients). The Supporting Information includes a detailed discussion of this analysis. We also performed global analysis using MATLAB (MathWorks) and the approach described by Patel et al. (*38*).

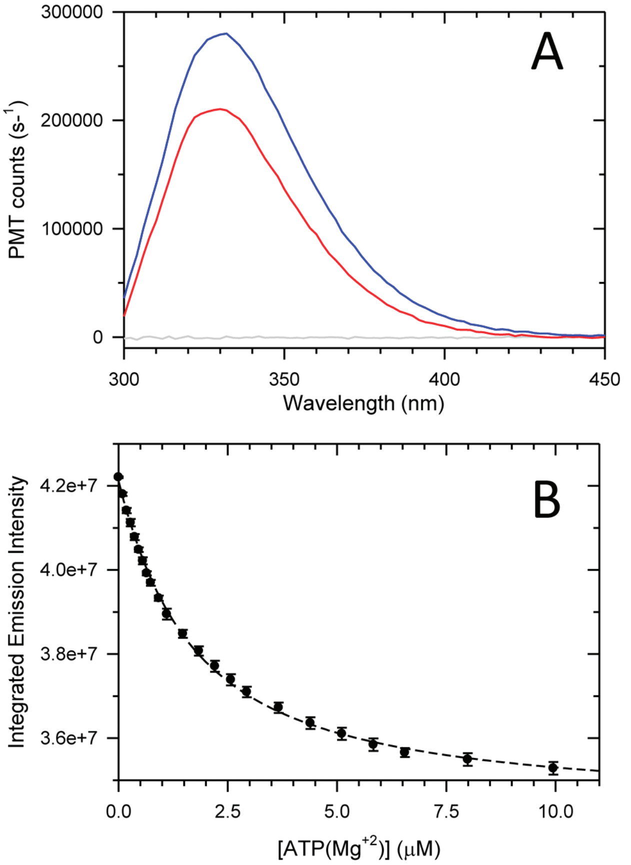

Figure 1: ATP(Mg^{2+}) binding to P4^{F487W}. (A) Emission spectra were recorded for 0.16 μM P4^{F487W} in the absence (blue) and presence (red) of 10 μM ATP for protein samples in TnM buffer at 4 °C. These spectra have been corrected by subtraction of a buffer-only emission spectrum collected under the same conditions in the same cuvette. The gray line shows a buffer-minus-buffer corrected spectrum (two different buffer samples). (B) Results of fluorescence-monitored titrations of P4^{F487W} with ATP. The integrated emission intensity (300−450 nm) was determined after each of a series of ATP additions to a 0.5 μM solution of P4^{F487W}. The dashed line shows the best fit of the data to a model with a single binding site (K_d = 1.5 μM) obtained using least-squares minimization in DynaFit (*51*). Error bars represent standard errors of the mean from three independent titrations.

RESULTS AND DISCUSSION

Affinity and Kinetics of ATP Binding to P4^{F487W}. To enable detection of ATP binding events, we introduced a F487 to W substitution into the F box of the active site of the P4 domain of *T. maritima* CheA. In previous work with *E. coli* CheA, an analogous substitution had little effect on the activity of the enzyme and provided a fluorescent reporter that responded to ATP binding events (*39*). We purified *T. maritima* P4^{F487W} (overproduced in *E. coli*) and analyzed the effect of ATP on its intrinsic fluorescence. Addition of ATP(Mg^{2+}) caused a decrease in this magnitude of the emission signal (Figure 1A). The maximal effect at saturating ATP concentrations was an approximately 25% reduction of the integrated emission signal intensity between 300 and 450 nm. Although this change is relatively small, it provided an adequate signal for monitoring formation of the P4^{F487W}·ATP(Mg^{2+}) complex in binding titrations using submicromolar concentrations of protein (Figure 1B). Analysis of the results of such titrations indicated a K_d of 1.5 μM for the P4^{F487W}·ATP(Mg^{2+}) complex at 4 °C. We used 4 °C for these titrations so that we could generate a K_d value under conditions identical to those used for the kinetics studies (below), which required low temperatures to slow the reactions. Analogous fluorescence-monitored titrations at 25 °C indicated a K_d of 10 μM (results not shown), comparable to the value (15 μM) determined previously by Bilwes et al. for Tm P4 using a chromatographic method (*17*).

To study the kinetics of ATP(Mg^{2+}) binding to P4^{F487W}, we used a stopped-flow fluorescence instrument to monitor time courses of ATP-induced fluorescence changes. We initiated reactions by rapidly mixing P4^{F487W} (final concentration of 5 μM) with a series of ATP solutions (final concentrations ranged from 1 to 1100 μM) in the stopped-flow instrument. Protein fluorescence decreased rapidly during the 100 ms following mixing; the rate and extent of this decrease were affected by ATP concentration (Figure 2A,B). Under pseudo-first-order conditions ([ATP] > 8[P4^{F487W}]), each

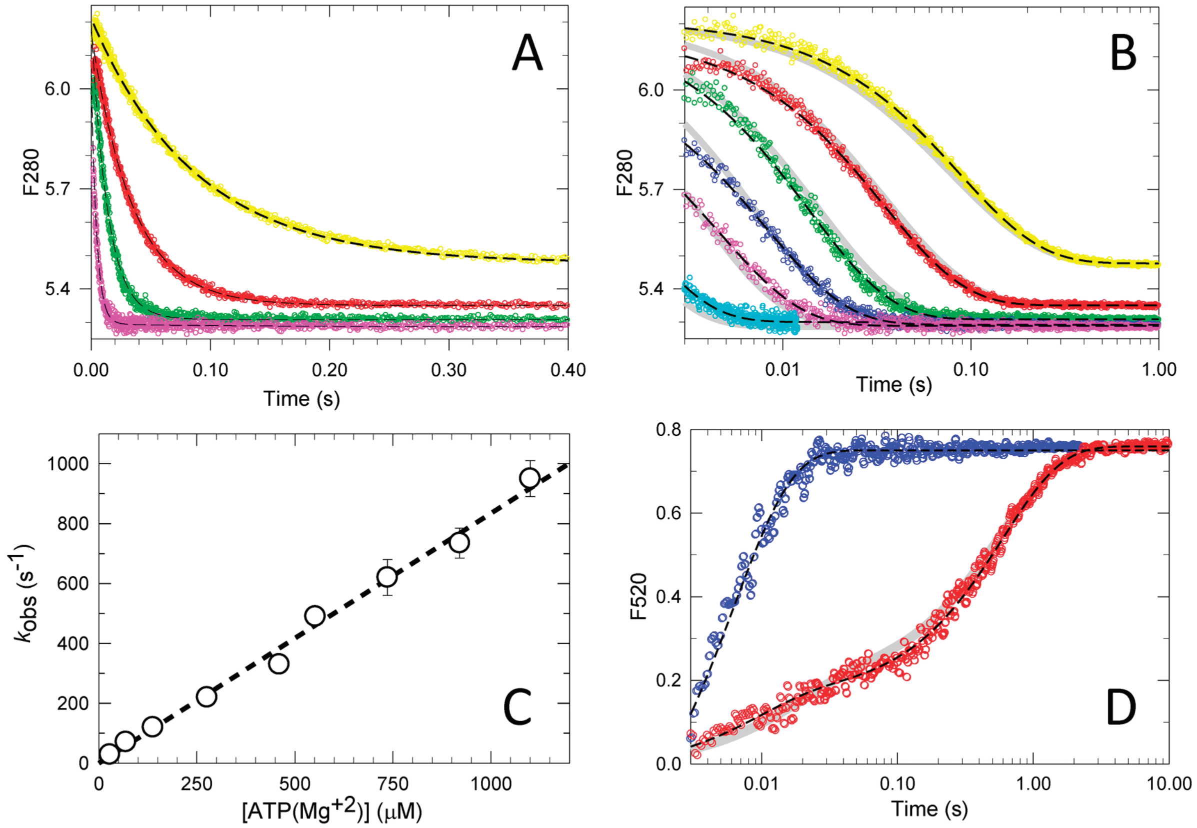

FIGURE 2: ATP association and dissociation kinetics. (A) The fluorescence emission signal of P4^{F487W} was monitored in a stopped-flow instrument after rapid mixing of equal volumes (40 μL) of 10 μM P4^{F487W} and ATP (10−2500 μM) in TnM buffer at 4 °C. A subset of these time courses is shown here: 12 μM (yellow), 30 μM (red), 70 μM (green), and 300 μM (pink) (concentrations postmixing). Data were recorded using a $\lambda_{\text{excitation}}$ of 280 nm and a $\lambda_{\text{emission}}$ of $>$ 335 nm. The dashed lines show the computer-generated best fits of each time course to a single-exponential decay, defining k_{observed} for the binding reaction at each ATP concentration. (B) ATP binding time courses plotted using a log scale x-axis: 12 μM (yellow), 30 μM (red), 70 μM (green), 150 μM (blue), 300 μM (pink), and 920 μM (cyan) (concentrations postmixing). For reactions with $<$ 500 μM ATP, 1000 logarithmically spaced data points were collected over a time span of 1 s. For reactions with $>$ 500 μM ATP, 1000 data points (linearly arrayed) were collected over 0.01 s. The dashed lines show the computer-generated best fits of each time course to a single-exponential decay, defining k_{observed} for the binding reaction at each ATP concentration. These values are plotted as a function of ATP concentration in panel C. The dashed line in panel C was determined by linear regression analysis (SigmaPlot) and has a slope of 0.83 μM^{-1} s^{-1}. (D) Kinetics of dissociation of ATP(Mg^{2+}) from P4^{F487W}. The fluorescence emission signal of TNP-ATP was monitored to follow formation of the P4^{F487W}·TNP-ATP(Mg^{2+}) complex for the reaction of 30 μM TNP-ATP with 5 μM free P4^{F487W} (blue data) and with 5 μM P4^{F487W} that had been preincubated with 3.5 μM ATP(Mg^{2+}) (red data). Dashed lines (black) show the computer-generated best fits of the data using a single-exponential equation (for free P^{4F487W}) or a two-exponential equation (for the P4^{F487W}/ATP mixture). Each time course shown in panels A, B, and D is an average of 10−15 replicate stopped-flow traces. In these same panels, the gray lines show computer-generated simulated time courses generated using rate constants and MFC values determined by global analysis using Global Kinetic Explorer to model a single-step reversible binding reaction.

time course could be fit well as a single-exponential decay,[2] yielding a pseudo-first-order rate constant (k_{observed}) at each ATP concentration. A plot of these k_{observed} values versus ATP concentration exhibits a linear relationship and indicates a second-order rate constant of 0.83 ± 0.07 μM^{-1} s^{-1} (Figure 2C). For a simple, one-step binding reaction, one expects $k_{\text{observed}} = k_{\text{off}} + k_{\text{on}} \times [\text{ATP}]$, so the y-axis intercept of the plot in Figure 2C would equal k_{off} (*35*, *40*, *41*). We observed that this intercept was very close to the origin (±2 s^{-1}), suggesting that the rate constant for dissociation is less than ~2 s^{-1}.

To explore ATP dissociation kinetics directly, we used TNP-ATP as a high-affinity trapping agent to capture P4^{F487W} as it was released from the P4^{F487W}·ATP(Mg^{2+}) complex (Figure 2D), as described previously (*39*) . The resulting P4^{F487W}·TNP-ATP-(Mg^{2+}) complex has a large fluorescence signal (see below) at wavelengths ($>$ 540 nm) where the intrinsic fluorescence of the protein and the absorbance properties of ATP do not interfere. In the absence of any ATP, the reaction between P4^{F487W} and 30 μM TNP-ATP(Mg^{2+}) took place rapidly ($k_{\text{observed}} \sim 160$ s^{-1}).[3] When this same solution of P4^{F487W} was pre-equilibrated with ATP-(Mg^{2+}) before being mixed with the same TNP-ATP solution, we observed a markedly biphasic time course: 20−25% of the fluorescence change took place in the fast phase ($k_{\text{observed}} \sim 150$ s^{-1}), and the remaining 75−80% of the fluorescence change took place in a slow phase with a k_{observed} of 1.7 s^{-1} (Figure 2D).

---

[2] At the lowest ATP concentrations (e.g., 12 and 30 μM in Figure 2A), a slight lag was apparent at the earliest time points. This could indicate that the ATP binding mechanism is more complicated than a single one-step reaction. For example, the observed lags could reflect the existence of a spectrally silent binding step generating a low-affinity complex prior to the step responsible for the F_{280} decrease. However, these deviations were small and were not observed under pseudo-first-order conditions, so we did not consider them further.

[3] This experiment used a $\lambda_{\text{excitation}}$ of 520 nm and monitored emission at wavelengths of $>$ 540 nm. Using these settings, the TNP-ATP binding reaction appears as a rapid, single-exponential increase. This differs somewhat from the biphasic time courses observed when $\lambda_{\text{excitation}}$ is set to 410 nm, which was done for the detailed analysis of TNP-ATP binding kinetics (Figures 4−7). By using a $\lambda_{\text{excitation}}$ of 520 nm, we simplified the analysis of the ATP dissociation time courses because we eliminated the need to take into account slow spectral changes arising from TNP-ATP binding.

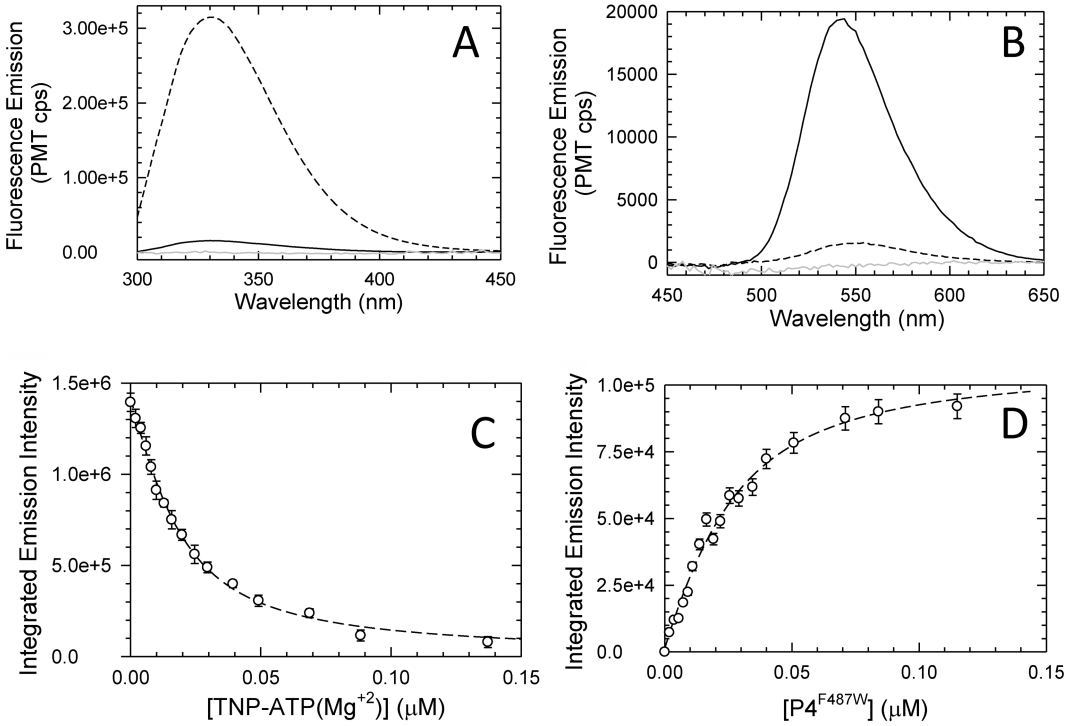

FIGURE 3: TNP-ATP(Mg^{2+}) binding to $P4^{F487W}$. (A) With a $\lambda_{excitation}$ of 280 nm, emission spectra were recorded for 0.186 μM $P4^{F487W}$ in the absence (---) and presence (black solid line) of 0.8 μM TNP-ATP. Shown here are buffer-corrected and dilution-corrected spectra for mixtures in TnM buffer at 4 °C. The gray line is a buffer-only control. (B) With a $\lambda_{excitation}$ of 410 nm, emission spectra were recorded for 0.192 μM TNP-ATP in the absence (---) and presence (solid black line) of 0.8 μM $P4^{F487W}$ for samples in TnM buffer at 4 °C. The gray line is for buffer alone. (C) Results of fluorescence-monitored titrations of $P4^{F487W}$ with TNP-ATP. The integrated emission intensity (300−450 nm) was determined after each of a series of additions of TNP-ATP to a 0.0186 μM solution of $P4^{F487W}$. The dashed line shows the best fit of the data to a model with a single binding site (K_d = 0.014 μM) obtained using least-squares minimization in DynaFit (*51*). Error bars represent standard errors of the mean from two independent titrations. (D) Results of fluorescence-monitored titrations of TNP-ATP with $P4^{F487W}$. The integrated emission intensity (450−650 nm) was determined after each of a series of additions of $P4^{F487W}$ to a 0.0192 μM solution of TNP-ATP. The dashed line shows the best fit of the data to a model with a single binding site (K_d = 0.016 μM) obtained using least-squares minimization in DynaFit (*51*). Error bars represent standard errors of the mean from two independent titrations.

Knowing the concentrations of $P4^{F487W}$ and ATP and the K_d of the protein·ATP complex, we expected the initial pre-equilibrated mixture to contain 70% of the P4 present as the P4·ATP(Mg^{2+}) complex and 30% as free $P4^{F487W}$. Therefore, when this mixture was exposed to TNP-ATP(Mg^{2+}), we expected that ~30% of the observed fluorescence change would take place rapidly (at ~160 s^{-1}) and that the remainder of the reaction (~70% of the observed amplitude) would take place at a rate dictated by the dissociation rate of the $P4^{F487W}$·ATP(Mg^{2+}) complex. Our observations match these predictions, indicating that the k_{off} for this complex is 1.7 s^{-1}. Similar values of k_{off} were observed when this experiment was repeated using higher TNP-ATP concentrations (60 and 100 μM) (results not shown).

The observed ATP association and dissociation kinetics are consistent with a simple one-step reversible binding mechanism:

$$P4 + ATP(Mg^{2+}) \underset{k_{off}}{\overset{k_{on}}{\rightleftharpoons}} P4 \cdot ATP(Mg^{2+}) \qquad \text{(Scheme 1)}$$

where k_{on} = 0.83 $\mu M^{-1}\,s^{-1}$ and k_{off} = 1.70 s^{-1}. For such a mechanism, $K_d = k_{off}/k_{on}$, so our kinetics results predict a K_d value of 2.0 μM which compares favorably with the value (1.5 μM) determined from equilibrium binding titrations (Figure 1B).

Tight Affinity and Rapid Kinetics of TNP-ATP(Mg^{2+}) Binding to $P4^{F487W}$. To explore the interaction of TNP-ATP(Mg^{2+}) with $P4^{F487W}$, we first examined (Figure 3) the effect of TNP-ATP(Mg^{2+}) on the intrinsic fluorescence of the protein (F_{280}) as well as on the emission properties of TNP-ATP (F_{410}). Binding of TNP-ATP resulted in an extensive decrease in the magnitude of the emission signal of $P4^{F487W}$ (> 95% reduction at saturating TNP-ATP concentrations) (Figure 3A) and caused a large increase in the magnitude of the emission signal of the TNP (Figure 3B), as described previously (*17*, *24*, *28*). Using these signals to monitor formation of the $P4^{F487W}$·TNP-ATP(Mg^{2+}) complex, we performed binding titrations to quantify the affinity of the interaction (Figure 3C,D). Analysis of these results indicated a K_d of 0.015 ± 0.001 μM, a value close to that reported previously for the complex of TNP-ATP with *T. maritima* P4 lacking the F487W substitution (*24*). These measurements indicate that the interaction of $P4^{F487W}$ with TNP-ATP is ~100-fold tighter than that for binding of unmodified ATP.

We used stopped-flow fluorescence experiments to monitor the rapid kinetics of the TNP-ATP(Mg^{2+}) binding reaction. Figure 4A shows a typical time course of TNP fluorescence change (F_{410}) observed after $P4^{F487W}$ had been mixed with TNP-ATP, and Figure 4B depicts the change in $P4^{F487W}$ intrinsic fluorescence (F_{280}) for this same reaction. The F_{410} and F_{280} time courses are both biphasic. This is readily observed in Figure 4A. The magnitude of the F_{410} signal increases rapidly over the first 30−40 ms, reaches a plateau, and then exhibits a small (~15%) decrease over the next ~200 ms. The F_{410} time courses could be fit well as the sum of two exponential processes (dashed line in Figure 4A). Because of the large rate difference between the fast and slow phases in these reactions, these data are best viewed using a log scale x-axis (Figure 4A, main panel). The biphasic nature of the binding reaction is also apparent, although less strikingly, in reactions monitoring F_{280} (Figure 4B). The time

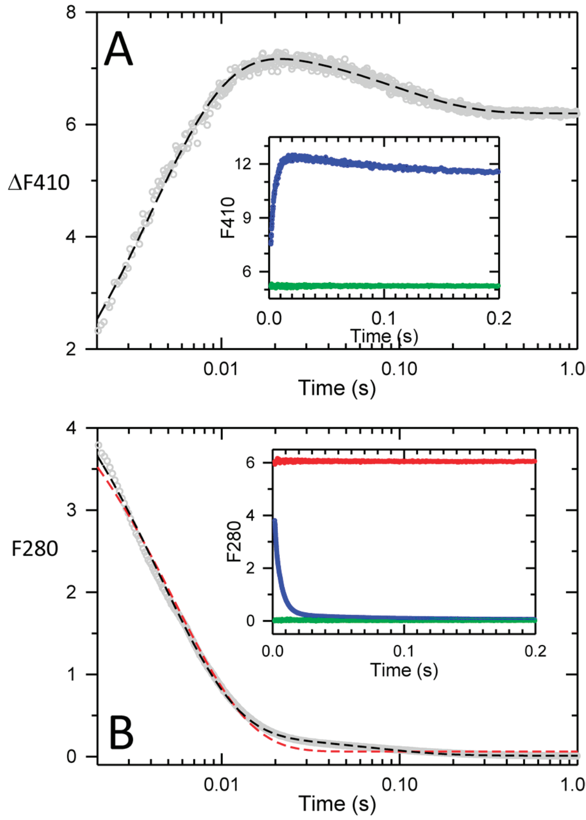

FIGURE 4: Biphasic time courses for the binding reaction between $P4^{F487W}$ and TNP-ATP(Mg^{2+}). Reaction time courses were monitored in a stopped-flow fluorescence instrument. Each time course is an average of 10−15 replicate stopped-flow traces. The units for the *y*-axes on these plots are PMT voltages. (A) The reaction between 5 μM $P4^{F487W}$ and 40 μM TNP-ATP (concentrations postmixing) was monitored by following the TNP fluorescence signal (F_{410}) in a stopped-flow instrument: $\lambda_{excitation}$ = 410 nm, and $\lambda_{emission}$ > 540 nm. The inset shows the F_{410} signal (after correction for inner filter effects) observed for 40 μM TNP-ATP in TnM buffer in the absence of $P4^{F487W}$ (green) and for 40 μM TNP-ATP in TnM buffer with 5 μM $P4^{F487W}$ (blue). The main panel shows the time course for this same binding reaction but using a log scale *x*-axis and after subtraction of the TNP-ATP baseline signal (5.2 V). The dashed line depicts the best computer-generated fit of the data to the sum of two exponential processes. (B) The reaction between 5 μM $P4^{F487W}$ and 40 μM TNP-ATP was monitored by following the $P4^{F487W}$ fluorescence signal (F_{280}) in a stopped-flow instrument: $\lambda_{excitation}$ = 280 nm, and $\lambda_{emission}$ > 335 nm. The inset shows the F_{280} signal (after correction for inner filter effects) observed for 40 μM TNP-ATP in the absence of $P4^{F487W}$ (green), for 5 μM $P4^{F487W}$ in the absence of TNP-ATP (red), and for 40 μM TNP-ATP with 5 μM $P4^{F487W}$ (blue). The main panel shows the time course for this same binding reaction but using a log scale *x*-axis. The dashed red line depicts the best computer-generated fit of the data to a single-exponential decay; the dashed black line depicts the best computer-generated fit of the data to the sum of two exponential decays.

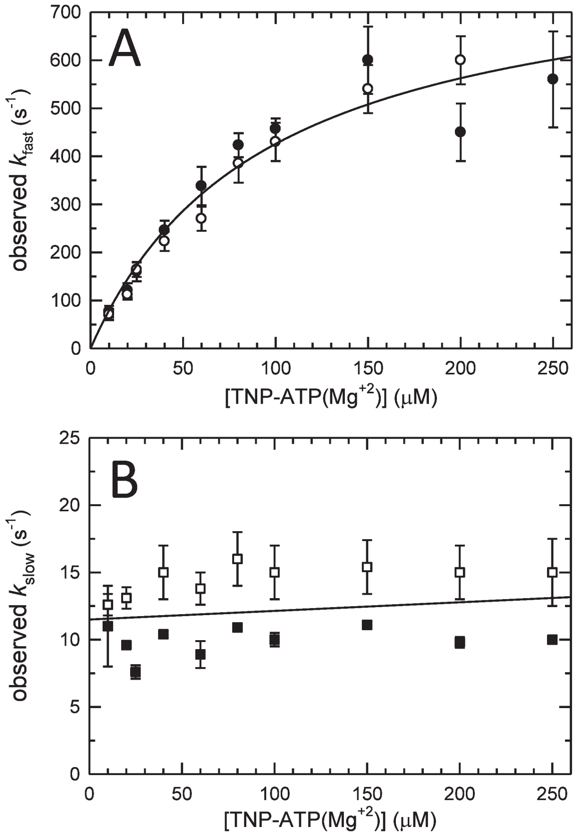

FIGURE 5: Analysis of the effect of TNP-ATP(Mg^{2+}) concentration on binding kinetics. Stopped-flow time courses for binding reactions performed under pseudo-first-order conditions were analyzed as the sum of two exponential processes (as in Figure 4) to define the observed rate constants for the fast and slow phases. (A) The observed k_{fast} values were determined by analysis of F_{410} time courses (●) and F_{280} time courses (○). The results indicate saturation kinetics and are fit by a three-parameter hyperbola (—) defined by a maximal extrapolated k_{fast} value of ~830 s^{-1} at saturating TNP-ATP concentrations, a half-maximal $k_{observed}$ value at ~95 μM TNP-ATP, and a *y*-axis intercept of ~0. (B) The observed k_{slow} values were determined by analysis of F_{410} time courses (■) and F_{280} time courses (□). The solid line was generated by linear regression and indicates that k_{slow} (~12.5 s^{-1}) is insensitive to TNP-ATP concentration. Error bars indicate the standard errors of the mean from two independent experiments.

course does not follow a single-exponential decay. Fitting this time course as a double-exponential markedly improved the agreement[4] between the observed and simulated time courses (σ_{FIT} = 0.057 for a one-exponential fit; σ_{FIT} = 0.0125 for a two-exponential fit).

We recorded time courses monitoring F_{410} and F_{280} for binding reactions at a series of TNP-ATP concentrations ranging from 1 to 200 μM (at higher concentrations, the rapid phase of the reaction was complete within the dead time of the stopped-flow instrument). Analysis of each fluorescence time course generated an observed rate constant for the rapid phase (k_{fast}) and for the second phase (k_{slow}); these values were similar for the F_{410}- and F_{280}-monitored reactions. For example, analysis of the F_{410} time courses in Figure 4A indicates k_{fast} = 246 s^{-1} and k_{slow} = 10.4 s^{-1}, while analysis of the F_{280} results in Figure 4B indicates k_{fast} = 225 s^{-1} and k_{slow} = 13 s^{-1}. Analysis of the effect of TNP-ATP concentration on the binding kinetics (Figure 5) indicates that k_{slow} is insensitive to this concentration and that k_{fast} exhibits a hyperbolic dependence on TNP-ATP concentration. The saturation kinetics observed for k_{fast} suggest that a binding step (with no or little fluorescence contribution) precedes the step responsible for the large increase in TNP fluorescence signal (i.e., the events contributing to k_{fast} comprise at least two steps). A third step (corresponding to k_{slow})

---

[4] The plot of residuals for this two-exponential fit indicates that it is not ideal, and a better fit was obtained when the time course was fit as a three-exponential process (Figure S2 of the Supporting Information). However, we decided to proceed with initial analysis of the F_{280} and F_{410} data as a two-exponential process for several reasons. First, the residuals for a biphasic fit were almost within the range of σ_{DATA} (Figure S2). Second, the rate constant indicated for the fastest phase in three-exponential fits was too fast to analyze accurately by stopped-flow methods ($k_{observed}$ > 1000 s^{-1} even at the lowest TNP-ATP concentrations). The possibility of a triphasic time course for the TNP-ATP(Mg^{2+}) binding reaction is reconsidered in Global Analysis of the ATP and TNP-ATP Binding Mechanisms.

then decreases the magnitude of the TNP emission signal by ~15%. Thus, the minimal reaction scheme that can account for our observations is a three-step sequential mechanism:

$$\mathrm{P4} + \mathrm{TNP\text{-}ATP(Mg^{2+})} \underset{k_{-1}}{\overset{k_{+1}}{\rightleftharpoons}} (\mathrm{Intermediate})_1$$

$$\underset{k_{-2}}{\overset{k_{+2}}{\rightleftharpoons}} (\mathrm{Intermediate})_2 \underset{k_{-3}}{\overset{k_{+3}}{\rightleftharpoons}} (\mathrm{FinalComplex}) \qquad \text{(Scheme 2)}$$

Analysis of Figure 5 can yield estimates of several of the rate constants in this mechanism, although this requires several assumptions (*35*, *40*, *41*). For example, if we assume that rapid equilibrium conditions apply ($k_{-1} \gg k_{+2}$) and that (Intermediate)$_1$ is spectrally silent, then the extrapolated maximal value of k_{fast} (~830 s^{-1}) represents k_{+2}; the concentration of TNP-ATP(Mg^{2+}) required to reach half-maximal k_{fast} (~95 μM) represents k_{-1}/k_{+1}, i.e., the K_d of the initial complex (Intermediate)$_1$; and k_{slow} (~12.5 s^{-1}) represents k_{+3} (or the sum of k_{+3} and k_{-3}). This interpretation, although simplistic, provided a starting point for the more rigorous analysis presented below (global analysis).

TNP-ATP Dissociation Kinetics. The results presented above provide little direct information about the reverse steps (k_{-1}, k_{-2}, and k_{-3}) in the TNP-ATP binding scheme. We performed two types of dissociation experiments to elucidate these steps. In both experiments, a large excess of ATP(Mg^{2+}) (nonfluorescent) was added to a mixture of the preformed P4$^{\mathrm{F487W}}$·TNP-ATP(Mg^{2+}) complex, and then the ensuing decrease in the magnitude of the TNP-ATP fluorescence signal (F_{410}) was monitored. We interpreted this decrease as resulting from dissociation of the P4$^{\mathrm{F487W}}$·TNP-ATP(Mg^{2+}) complex to generate free P4$^{\mathrm{F487W}}$ which was then quickly sequestered by the excess ATP. In the first dissociation experiment, a mixture of P4$^{\mathrm{F487W}}$ and TNP-ATP that had equilibrated for 5 min was introduced into one syringe of the stopped-flow instrument while a 200 mM solution of ATP(Mg^{2+}) was placed in the second syringe. When the instrument mixed together aliquots of these solutions, a decrease in the magnitude of the F_{410} signal was observed (Figure 6A). In Scheme 2, this experiment would correspond to monitoring dissociation of the (Final Complex) back to (Intermediate)$_2$ and then to (Intermediate)$_1$ and then finally to free P4$^{\mathrm{F487W}}$. Results of this experiment (Figure 6A) indicated a single-exponential time course and a rate constant of 0.13 s^{-1} for the overall dissociation process. Very similar results (not shown) were obtained when lower concentrations of ATP(Mg^{2+}) (50 and 100 mM) were used to trap the dissociated P4$^{\mathrm{F487W}}$, an observation that supported the assumption that the ATP trapping step was rapid compared to TNP-ATP dissociation.

We also used double-mixing stopped-flow experiments to examine the TNP-ATP dissociation reaction. These experiments allowed us to examine the dissociation properties of (Intermediate)$_2$ prior to its conversion to (Final Complex) and were undertaken to generate a more accurate estimate of k_{-2} than was possible using the single-mix dissociation experiments described above. For our experiments, P4$^{\mathrm{F487W}}$ was rapidly mixed with TNP-ATP-(Mg^{2+}) in mixer-1 of the stopped-flow instrument, and this mixture was allowed to age for a specified time interval, T_1 (6−250 ms), before being mixed with a very high concentration of ATP(Mg^{2+}) in mixer-2; then this P4/TNP-ATP(Mg^{2+})/ATP mixture was quickly pushed into the stopped-flow observation cell. Figure 6B shows some representative fluorescence time courses observed in double-mixing experiments. When T_1 was short (< 150 ms), these dissociation time courses were markedly biphasic, with a k_{fast} of ~14 s^{-1} and a k_{slow} of ~0.12 s^{-1}. As T_1 became longer, k_{fast} and k_{slow} were unchanged, but the contribution of the fast phase to the overall observed fluorescence change decreased progressively; when $T_1 \geq 250$ ms, the entire time course took place on a time

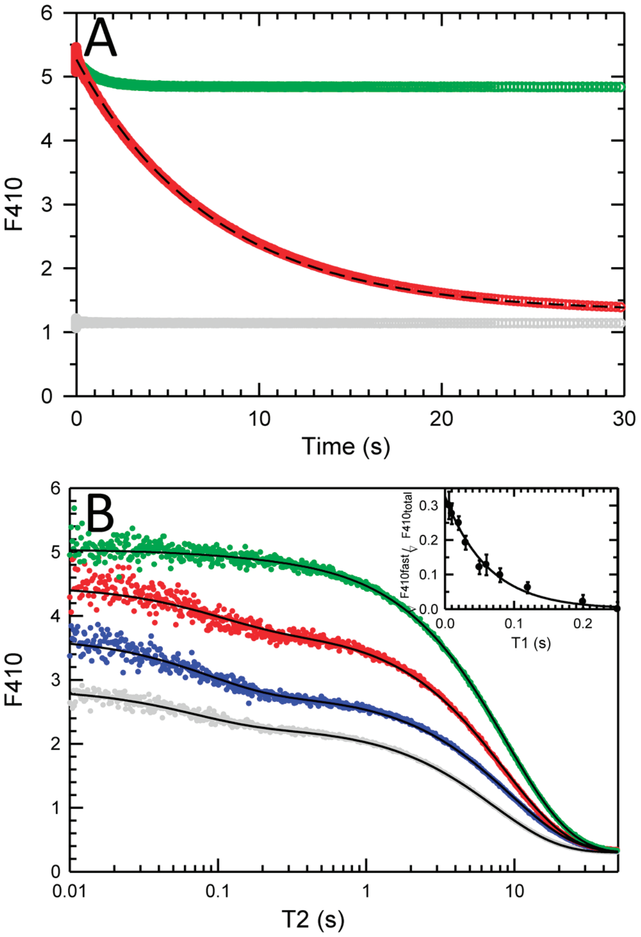

FIGURE 6: Dissociation kinetics for the P4$^{\mathrm{F487W}}$·TNP-ATP(Mg^{2+}) complex. A stopped-flow instrument was used to monitor the decrease in the magnitude of the fluorescence signal (F_{410}) due to the P4$^{\mathrm{F487W}}$·TNP-ATP(Mg^{2+}) complex observed after the complex was mixed with a large excess of nonfluorescent competitor ATP(Mg^{2+}) ($\lambda_{\mathrm{excitation}}$ = 410 nm, and $\lambda_{\mathrm{emission}}$ > 540 nm). (A) Red circles show the time course observed immediately after a 200 mM solution of ATP (with 200 mM MgCl$_2$) was mixed 1:1 with a pre-equilibrated solution containing 6.6 μM P4$^{\mathrm{F487W}}$ and 40 μM TNP-ATP (premixing concentrations) in TnM buffer. The dashed line is the computer-generated best fit of this time course to a single-exponential decay indicating a k_{observed} of 0.13 s^{-1}. Time courses for two control experiments are also shown. Green circles show the time course observed when the same 6.6 μM P4$^{\mathrm{F487W}}$/40 μM TNP-ATP solution was mixed 1:1 with buffer containing 200 mM MgCl$_2$, and gray circles show the signal observed when a 40 μM TNP-ATP solution (no P4$^{\mathrm{F487W}}$) was mixed 1:1 with buffer containing 200 mM MgCl$_2$. (B) Results from double-mixing experiments in which 13.2 μM P4$^{\mathrm{F487W}}$ was first rapidly mixed (in the stopped-flow instrument) 1:1 with 80 μM TNP-ATP in TnM buffer and then allowed to age for a specified interval (T_1), and then this P4$^{\mathrm{F487W}}$/TNP-ATP(Mg^{2+}) solution was mixed with 200 mM ATP (with 200 mM MgCl$_2$) and introduced into the stopped-flow observation chamber. The time following this second mixing event is defined as T_2. The main panel shows time courses collected for T_1 values of 0.006 s (gray circles), 0.01 s (blue circles), 0.03 s (red circles), and 0.25 s (green circles). The line through each set of data points represents the computer-generated best fit to a sum of two exponential decays, and this fit indicated values for k_{fast} and k_{slow} as well as the relative contributions of the fast and slow phases to the overall amplitude (F_{410}) of the reaction. The inset indicates that the relative contribution of the fast phase to the overall amplitude decreases as T_1 becomes longer. The line in this plot shows that a single-exponential decay describes this effect, and it indicated k_{observed} ~ 15 s^{-1}. Error bars represent standard errors of the mean from two independent experiments.

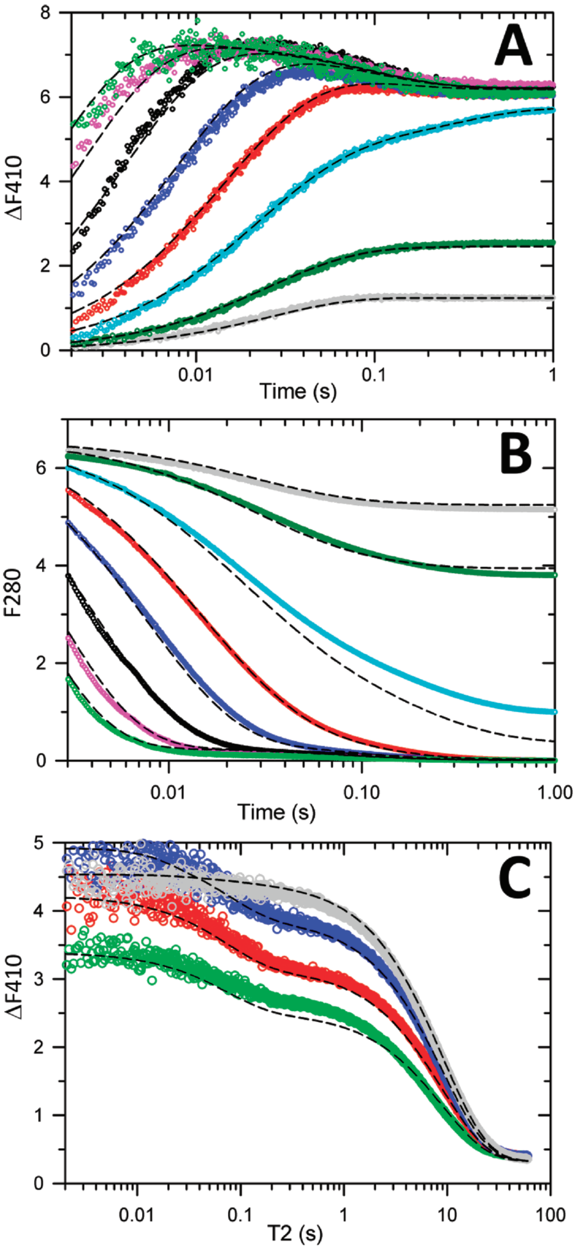

FIGURE 7: Computer simulations of reaction time courses for TNP-ATP binding and dissociation. A data set including 10 TNP-ATP binding time courses, two single-mix dissociation time courses, and nine double-mixing dissociation time courses was fit by global analysis to generate a set of six rate constants (Table 1, Constants from Global Analysis: Scheme 2) and four MFC values (detailed in the Supporting Information). Computer-generated simulations (dashed lines) using these constants are compared to a representative subset of the data: for TNP-ATP binding reactions monitored using F_{410} (A) and F_{280} (B) as well as for TNP-ATP dissociation reactions (C). In panels A and B, the TNP-ATP concentrations were 1 μM (gray), 2 μM (dark green), 5 μM (cyan), 10 μM (red), 20 μM (blue), 40 μM (black), 80 μM (pink), and 150 μM (green). In panel C, the dissociation reactions were examined in double-mixing experiments with T_1 set to 0.006 s (green), 0.010 s (red), 0.030 s (blue), and 0.250 s (gray).

scale reflecting k_{slow}. We interpreted these results in relation to Scheme 2. When $T_1 \leq 10$ ms, the first mixing step generated a mixture of 25−30% (Intermediate)$_2$ and 70−75% (Final Complex). (Intermediate)$_2$ could dissociate quickly ($k \sim 14$ s^{-1}), but (Final Complex) required considerably longer to achieve dissociation ($k \sim 0.12$ s^{-1}). As T_1 became >10 ms, more of the (Intermediate)$_2$ had a chance to convert to (Final Complex) before the ATP was added in the second mixing step, so the contribution of the fast phase to the overall amplitude of the reaction decreased, although the magnitudes of k_{fast} and k_{slow} remained unchanged. A plot of the relative contribution (% of overall amplitude) of the fast phase as a function of T_1 (Figure 6B, inset) indicated that, during the T_1 interval, (Intermediate)$_2$ converted to Final Complex with a rate constant of ~15 s^{-1}. In relation to Scheme 2, we preliminarily interpreted the rate constant for this conversion as corresponding to k_{+3}, while the rate constants for the fast (14 s^{-1}) and slow (0.12 s^{-1}) phases of each individual time course in Figure 6B corresponded to k_{-2} and k_{-3}, respectively. Below, we discuss a more rigorous analysis of these results indicating that these preliminary assignments for k_{-2} and k_{-3} were incorrect.

Global Analysis of the ATP and TNP-ATP Binding Mechanisms. The overall goals for each of our two kinetic analyses (ATP and TNP-ATP) were (i) to propose a model that specifies the minimal number of steps to account for our observations and (ii) to define the values of the rate constants for as many steps as possible in this model. To achieve these goals, we employed a two-stage approach (*36*, *37*, *42*): initial conventional analysis (described above) followed by global analysis (described briefly here and in more detail in the Supporting Information). Conventional analysis was useful for defining the basic reaction mechanism (number of steps) and for providing initial estimates of the rate constants for each step. However, as noted by Johnson (*36*, *37*) and others (*38*, *43*, *44*), conventional analysis ignores some of the information content in kinetic data (e.g., reaction amplitudes) and does not facilitate integration of multiple kinds of kinetic data (e.g., binding data and dissociation data), so it is important to supplement conventional analysis with some kind of global analysis that can overcome these limitations. This is especially true for multistep reaction mechanisms that can give rise to nonintuitive results. Moreover, global analysis has the ability to determine how well the extracted rate constants are constrained by the data.

Analysis of the ATP binding reaction was straightforward: our results were consistent with a simple one-step reaction mechanism, and estimates of kinetic constants could be extracted from kinetic results by simple graphical analysis (Figure 2) (*35*, *40*, *41*). To corroborate this conventional analysis, we subjected our results to global analysis using KinTek Global Kinetic Explorer (*36*). The following kinetic parameters were extracted in this analysis: $k_{+1} = 0.92 \pm 0.08$ μM^{-1} s^{-1}, and $k_{-1} = 1.9 \pm 0.4$ s^{-1}. Using these parameters, computer simulations of time courses match the data well (Figure 2B). The Supporting Information includes a discussion of the statistical assessment of this fit.

Binding of TNP-ATP(Mg^{2+}) to P4$^{\text{F487W}}$ involves at least three sequential steps (Scheme 2), so extracting the values of individual rate constants was more difficult than for the ATP binding reaction. Conventional analysis required simplifying assumptions (*36*, *37*, *41*) to enable estimation of the rate constants for the forward and reverse reactions for each of the three steps, as described above. These values are listed in Table 1. To improve these estimates, we used the DataFit utility of Global Kinetic Explorer. This analysis indicated that it is not possible to extract accurate estimates of the rate constants for k_{+1} or k_{-1}, although the ratio of these values is ~130 μM, and the upper and lower bounds were defined. To enable further analysis, we set k_{+1} at the diffusion limit (100 μM^{-1} s^{-1}) and then proceeded to define the best fit values for the rest of the rate constants and the molar fluorescence coefficients of the intermediates. The final set of values generated through this analysis is listed in Table 1 as Rate

Table 1: Rate Constants for the Reaction of TNP-ATP with P4^{F487W}

k_{+1}	k_{-1}	k_{+2}	k_{-2}	k_{+3}	k_{-3}
(A) Rate Constants from Conventional Analysis: Scheme 2[a]					
{100 μM^{-1} s^{-1}}[b]	{9500 s^{-1}}[b]	830 s^{-1} (±80[c])	14 s^{-1} (±0.2[c])	13 s^{-1} (±2[c])	0.25 s^{-1} (±0.04[c])
(B) Rate Constants from Global Analysis: Scheme 2[d]					
{100 μM^{-1} s^{-1}}[b]	{13000 s^{-1} (±5000[e])}	1100 s^{-1} (±400[e])	2.5 s^{-1} (±0.2[e])	11.1 s^{-1} (±0.3[e])	0.62 s^{-1} (±0.04[e])
(C) Rate Constants from Global Analysis: Scheme 3[f]					
480 s^{-1} UB[g]	160 s^{-1} UB[g]	10 μM^{-1} s^{-1} (±7[d])	2.2 s^{-1} UB[g]	10.8 s^{-1} UB[g]	0.61 s^{-1} (±0.03[d])

[a] Binding data were analyzed assuming a rapid equilibrium model using graphical methods described previously (*41*) and in the text. [b] For Scheme 2, values of k_{+1} and k_{-1} are not well constrained by the data; to enable further analysis, we set k_{+1} at the diffusion limit and then k_{-1} was either calculated (conventional analysis) or defined by regression analysis (global analysis) to account for the observed saturation kinetics. [c] Standard error reported by the fitting program (SigmaPlot). [d] Thirty-one separate time courses were analyzed using Global Kinetic Explorer assuming that the binding reaction is best represented by Scheme 2. Each time course (1000 time points) was the average of 10−15 stopped-flow traces. [e] Upper and lower bounds were defined by the fitting program (Global Kinetic Explorer) as values that caused a < 20% increase in χ^2 above the minimum value observed with the best-fit parameters. These bounds were used to assign the uncertainties (±) reported here. For example, the upper and lower bounds for k_{+2} are 700 and 1500 s^{-1}, respectively. [f] Thirty-one separate time courses were analyzed using Global Kinetic Explorer assuming that the binding reaction is best represented by Scheme 3. Each time course (1000 time points) was the average of 10−15 stopped-flow traces. [g] UB denotes unbounded: the fitting program (Global Kinetic Explorer) was unable to define an upper or lower bound using the same criteria detailed in footnote c. This indicates that these rate constants are not well constrained by the data.

Constants from Global Analysis: Scheme 2. In a comparison of these rate constants to those determined by conventional analysis, the most notable differences are in k_{-2} and k_{-3}. When the set of rate constants from global analysis was used in computer simulations, the predicted reaction time courses matched the experimental results well (Figure 7). This agreement was considerably better than that observed using the rate constants from conventional analysis (Figure S3 and Table S2 of the Supporting Information). The Supporting Information includes a discussion of the statistical assessment of these fits.

Although visual inspection of the fits depicted in Figure 7 indicated close agreement between the simulated and experimental time courses for most of the experiments, there were differences in some of the time courses (the Supporting Information includes a statistical analysis of the goodness of fit). We considered several possible explanations for these differences. One possibility is that we were incorrect (or overoptimistic) in assuming that a single set of rate constants could represent, with high accuracy, both the signal that monitored ligand events (F_{410}) and the signal that monitored the protein during binding (F_{280}). Any of the "single" steps (arrows) of Scheme 2 might, in fact, reflect several discrete events that we can, at our current level of resolution, observe only as a composite. Depending on how these discrete events contribute to the observed spectral changes, one might expect to obtain slightly different values for the overall rate constant for the composite depending on whether the ligand or protein signals were being monitored. In this regard, it is interesting to note that the results presented in Figure 5 do indicate small differences between the k_{fast} and k_{slow} values observed for the F_{410} and F_{280} signals. Note, for example, that the average k_{slow} is ~9.5 s^{-1} for the F_{410} results and ~14.5 s^{-1} for the F_{280} results. By forcing the fitting program to choose a single rate constant to represent both the F_{410} and F_{280} results, we may have limited the overall success of the fitting exercise, at least from the perspective of χ^2 minimization.

Another possible explanation for why our best fits were not better is that the model we were fitting (Scheme 2) was inaccurate. In this scheme, the observed saturation kinetics for the fast phase in TNP-ATP binding results from a bimolecular ligand binding step preceding the step responsible for the large fluorescence increase. This latter step is unimolecular and might reflect, for example, a conformational change in the ligand-bound active site; it becomes rate-limiting at sufficiently high ligand concentrations. This is the traditional way of explaining saturation kinetics, but it is not the only way (*35*, *40*, *41*). An alternative reaction mechanism worth considering is Scheme 3.

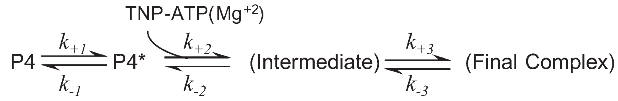

In this scheme, a protein conformational change precedes ligand binding; this first step becomes rate-limiting at a sufficiently high ligand concentration. We used Global Kinetic Explorer to find the best-fit set of rate constants for our TNP-ATP data set according to Scheme 3 (Table 1). The reaction time courses predicted by these rate constants were very similar to those generated by applying Scheme 2, and statistical analysis (Supporting Information) indicated that Scheme 2 and Scheme 3 were approximately equal in their ability to model the TNP-ATP binding and dissociation data.

Of course, another way to improve the goodness of fit is to include an additional step in the reaction scheme, expanding it from a three-step reaction to four sequential steps. However, in the absence of any compelling evidence for such an additional step (i.e., beyond the lack of a statistically satisfying outcome), we chose not to follow up on this option.

SUMMARY AND CONCLUSIONS

One general conclusion from this work is that the minimal reaction scheme necessary to accurately describe ATP(Mg^{2+}) binding by P4^{F487W} is very simple, a single reversible step. This finding was somewhat surprising because our previous work with the corresponding F-to-W substitution mutant of *E. coli* CheA had indicated a two-step mechanism for ATP(Mg^{2+}) binding (*39*). This difference may indicate that the ATP binding sites of *T. maritima* and *E. coli* CheA operate somewhat differently despite employing a very similar arrangement of active site determinants. Alternatively, *Tm*P4 might, in fact, utilize a two-step binding mechanism, but with the first step having such a low affinity that it precluded detection of saturation kinetics.

In addition to this difference, *T. maritima* CheA differs from its *E. coli* counterpart by having a tighter affinity for ATP(Mg^{2+}) (K_d of 1.5 μM vs 40 μM at 4 °C). Our results indicate that this affinity difference primarily reflects the slower dissociation kinetics for the *T. maritima* CheA·ATP(Mg^{2+}) complex; the association rate constants for ATP binding to the *T. maritima* and *E. coli* proteins are comparable (0.9 and 0.7 $\mu M^{-1}\ s^{-1}$, respectively).

A second general conclusion arising from our kinetic analyses is that the binding mechanism for TNP-ATP(Mg^{2+}) is considerably more complicated than the simple one-step mechanism observed for ATP(Mg^{2+}) binding. At least three sequential steps are necessary to account for the observed kinetics of TNP-ATP(Mg^{2+}) binding and dissociation. What is taking place in these three steps? We considered two alternative reaction schemes. In Scheme 2, the first step generates a low-affinity complex. The kinetics of this step are not well-defined, as our results allow us only to estimate lower limits (e.g., a lower limit for k_{+1} is ~13 $\mu M^{-1}\ s^{-1}$). The second step of the TNP-ATP(Mg^{2+}) binding reaction takes place rapidly ($k \sim 1100\ s^{-1}$) and generates a large increase in the emission intensity of the TNP fluorophore; this likely results from the TNP group entering a more hydrophobic environment (*45*), such as the pocket occupied by TNP in the crystal structure of the P4·TNP-ATP complex (*17*), although it is also possible that TNP−water interactions are involved (*46*). The equilibrium constant for this step is large (> 400), indicating that it involves formation of energetically favorable binding contacts. Step 3 is also favorable ($K_{eq} \sim 18$) but considerably slower ($k \sim 11\ s^{-1}$) than step 2 and causes the TNP emission intensity to decrease slightly, perhaps indicating a shift in the position of the TNP group or the orientation of some active site group that changes the environment of the TNP. The combined effect of steps 2 and 3 is to convert a relatively low-affinity, low-fluorescence complex to a high-affinity, high-fluorescence one.

In the alternative binding mechanism of Scheme 3, the first step changes the protein (or ligand) from a binding-incompetent state to a binding-competent conformation. This might, for example, involve rearrangement of active site components such as the ATP-lid region (*17*, *18*) to make the active site (or the adjacent hydrophobic TNP binding pocket) accessible to the TNP-ATP. This event would be followed by ligand binding (step 2) and then a conformational shift (step 3).

Our current data set does not allow us to determine which of the two alternative schemes (Scheme 2 or Scheme 3) better describes the TNP-ATP(Mg^{2+}) binding reaction. This is not because of a lack of effort or low-quality data, but rather because the information content that can be extracted from these mechanisms is not sufficient: both mechanisms involve multiple steps, some of which do not generate an observable signal, while other steps are either too rapid to monitor accurately or take place at rates that are very similar to that of some other step. Further elucidation of the binding mechanism would require applying additional experimental approaches.

The detailed kinetic analysis presented here focuses on a simple situation, a monomeric protein domain binding ATP (or TNP-ATP) at a single active site. This analysis may facilitate future efforts aimed at understanding how CheA functions in more complicated scenarios. For example, in living bacterial cells, CheA functions as a dimer with two active sites, and these sites are regulated by membrane-associated receptor proteins using a mechanism that is not well understood. In future work, we hope to examine how these scenarios might affect the ATP binding kinetics of the CheA active site.

How might a detailed understanding of inhibitor binding kinetics provide useful information? In this regard, it is worth noting that experiments and computer modeling studies (*47*−*49*) suggest that the rate constant of the dissociation reaction for different inhibitors plays an important role in determining the efficacy of those inhibitors as drugs. In fact, for some drug targets, dissociation kinetics play a more important role than the overall affinity of the drug−protein complex or the binding rate of the drug does. Thus, having an understanding of the CheA−TNP-ATP interaction mechanism and the kinetics of the dissociation steps could be useful for the design of inhibitors that effectively target PHKs.

We made extensive use of global analysis to extract accurate estimates of rate constants and to assess how well our data constrained these values. The benefits of using computer simulations to support and extend conventional kinetic analysis have been recognized since the 1970s, but this approach did not become "mainstream" because it required prohibitive levels of computer expertise and hardware. With recent advances in personal computer speed and the availability of powerful but user-friendly software packages, these barriers have been largely eliminated (*36*−*38*, *44*, *50*, *51*), enabling what Johnson and coworkers have termed the "New Enzymology". This new level of analysis has provided some sobering examples of how conventional analysis, in the absence of any accompanying global analysis, can be extremely misleading (*36*, *37*). Our analysis of the TNP-ATP binding mechanism certainly corroborates two of the main points made by Johnson: experimental conditions can easily create situations that run counter to the simplifying assumptions necessary for conventional analysis, and multistep mechanisms can give rise to results that are difficult to interpret (or even counterintuitive). Computer modeling was a necessary tool for understanding how our kinetic observations related to possible reaction mechanisms.

ACKNOWLEDGMENT

We thank Drs. Sang-Youn Park and Brian Crane for plasmids and Dr. Dorothy Beckett for helpful discussions. Dr. Joseph Kolesar provided invaluable assistance with MATLAB. Ebele Okwumabua purified some of the protein used for this work, and Kristin Feelemyer helped to create the $P4^{F487W}$ substitution mutant.

SUPPORTING INFORMATION AVAILABLE

Detailed discussion of conventional and global analysis of ATP and TNP-ATP binding kinetics, including five figures and two tables: σ analysis for fitting of ATP binding time courses (Figure S1), σ analysis for fitting of TNP-ATP binding time courses (Figure S2), comparison of goodness of fit using rate constants from conventional and global analysis (Figure S3), triphasic nature simulated F_{280} time courses (Figure S4), confidence contours for the global fit of TNP-ATP binding and dissociation reactions according to Scheme 2 (Figure S5), kinetic parameters for the reaction of $P4^{F487W}$ with ATP (Table S1), and kinetic parameters for the reaction of $P4^{F487W}$ with TNP-ATP (Table S2). This material is available free of charge via the Internet at http://pubs.acs.org.

REFERENCES

1. Bourret, R. B., and Silversmith, R. E. (2010) Two-component signal transduction. *Curr. Opin. Microbiol. 13*, 113–115.

2. Hoch, J. A., and Silhavy, T. J. (1995) Two-component signal transduction, American Society for Microbiology Press, Washington, DC.
3. Hess, J. F., Oosawa, K., Matsumura, P., and Simon, M. I. (1987) Protein phosphorylation is involved in bacterial chemotaxis. *Proc. Natl. Acad. Sci. U.S.A. 84*, 7609–7613.
4. Parkinson, J. S. (1976) *cheA*, *cheB*, and *cheC* genes of *Escherichia coli* and their role in chemotaxis. *J. Bacteriol. 126*, 758–770.
5. Swanson, R. V., Sanna, M. G., and Simon, M. I. (1996) Thermostable chemotaxis proteins from the hyperthermophilic bacterium *Thermotoga maritima*. *J. Bacteriol. 178*, 484–489.
6. Wadhams, G. H., and Armitage, J. P. (2004) Making sense of it all: Bacterial chemotaxis. *Nat. Rev. Mol. Cell Biol. 5*, 1024–1037.
7. Hess, J. F., Bourret, R. B., and Simon, M. I. (1988) Histidine phosphorylation and phosphoryl group transfer in bacterial chemotaxis. *Nature 336*, 139–143.
8. Sanders, D. A., Gillece-Castro, B. L., Stock, A. M., Burlingame, A. L., and Koshland, D. E., Jr. (1989) Identification of the site of phosphorylation of the chemotaxis response regulator protein, CheY. *J. Biol. Chem. 264*, 21770–21778.
9. McCleary, W. R., and Stock, J. B. (1994) Acetyl phosphate and the activation of two-component response regulators. *J. Biol. Chem. 269*, 31567–31572.
10. Welch, M., Oosawa, K., Aizawa, S.-I., and Eisenbach, M. (1994) Effects of phosphorylation, Mg^{2+}, and conformation of the chemotaxis protein CheY on its binding to the flagellar switch protein FliM. *Biochemistry 33*, 10470–10476.
11. Eisenbach, M. (1996) Control of bacterial chemotaxis. *Mol. Microbiol. 20*, 903–910.
12. Anand, G. S., and Stock, A. M. (2002) Kinetic basis for the stimulatory effect of phosphorylation on the methylesterase activity of CheB. *Biochemistry 41*, 6752–6760.
13. Sourjik, V., and Berg, H. C. (2002) Binding of the *Escherichia coli* response regulator CheY to its target measured in vivo by fluorescence resonance energy transfer. *Proc. Natl. Acad. Sci. U.S.A. 99*, 12669–12674.
14. Sourjik, V., and Berg, H. C. (2002) Receptor sensitivity in bacterial chemotaxis. *Proc. Natl. Acad. Sci. U.S.A. 99*, 123–127.
15. Kollmann, M., Lovdok, L., Bartholome, K., Timmer, J., and Sourjik, V. (2005) Design principles of a bacterial signalling network. *Nature 438*, 504–507.
16. Bilwes, A., Alex., L., Crane, B. R., and Simon, M. I. (1999) Structure of CheA, a signal-transducing histidine kinase. *Cell 96*, 131–141.
17. Bilwes, A., Quezada, C. M., Croal, L. R., Crane, B. R., and Simon, M. I. (2001) Nucleotide binding by the histidine kinase CheA. *Nat. Struct. Biol. 8*, 353–360.
18. Bilwes, A. M. P., Quezada, C. M., Simon, M., and Crane, B. R. (2003) Structure and function of CheA, the histidine kinase central to bacterial chemotaxis. In Histidine Kinases in Signal Transduction, pp 48−74, Academic Press, San Diego.
19. Park, S.-Y., Quezada, C. M., Bilwes, A. M., and Crane, B. R. (2004) Subunit exchange by CheA histidine kinases from mesophile *Escherichia coli* and the thermophile *Thermotoga maritima*. *Biochemistry 43*, 2228–2240.
20. Quezada, C. M., Gradinaru, C., Simon, M. I., Bilwes, A. M., and Crane, B. R. (2004) Helical shifts generate two distinct conformers in the atomic resolution structure of the CheA phosphotransferase domain from *Thermotoga maritima*. *J. Mol. Biol. 341*, 1283–1294.
21. Quezada, C. M., Hamel, D. J., Gradinaru, C., Bilwes, A. M., Dahlquist, F. W., Crane, B. R., and Simon, M. I. (2005) Structural and chemical requirements for histidine phosphorylation by the chemotaxis kinase CheA. *J. Biol. Chem. 280*, 39581–30585.
22. Swanson, R. V., Schuster, S. C., and Simon, M. I. (1993) Expression of CheA fragments which define domains encoding kinase, phosphotransfer, and CheY binding activities. *Biochemistry 32*, 7623–7629.
23. Morrison, T. B., and Parkinson, J. S. (1994) Liberation of an interaction domain from the phosphotransfer region of CheA, a signaling kinase of *Escherichia coli*. *Proc. Natl. Acad. Sci. U.S.A. 91*, 5485–5489.
24. Eaton, A. K., and Stewart, R. C. (2009) The two active sites of *Thermotoga maritima* CheA dimers bind ATP with dramatically different affinities. *Biochemistry 48*, 6412–6422.
25. Gao, R., and Stock, A. M. (2009) Biological insights from structures of two-component proteins. *Annu. Rev. Microbiol. 63*, 133–154.
26. Okada, A., Gotoh, Y., Watanabe, T., Furuta, E., Yamamoto, K., and Utsumi, R. (2007) Targeting two-component signal transduction: A novel drug discovery system. *Methods Enzymol. 422*, 386–395.
27. Stephenson, K., and Hoch, J. A. (2004) Developing inhibitors to selectively target two-component and phosphorelay signal transduction systems of pathogenic microorganisms. *Curr. Med. Chem. 11*, 765–773.
28. Stewart, R. C., VanBruggen, R., Ellefson, D. D., and Wolfe, A. J. (1998) TNP-ATP and TNP-ADP as probes of the nucleotide binding site of CheA, the histidine protein kinase in the chemotaxis signal transduction pathway of *Escherichia coli*. *Biochemistry 37*, 12269–12279.
29. Plesniak, L., Horiuchi, Y., Sem, D., Meinenger, D., Stiles, L., Shaffer, J., Jennings, P. A., and Adams, J. A. (2002) Probing the nucleotide binding domain of the osmoregulator EnvZ using fluorescent nucleotide derivatives. *Biochemistry 41*, 13876–13882.
30. Grubmeyer, C., and Penefsky, H. S. (1981) The presence of two hydrolytic sites on beef heart mitochondrial adenosine triphosphate. *J. Biol. Chem. 256*, 3718–3727.
31. Hiratsuka, T., and Uchida, K. (1973) Preparation and properties of 2′(or3′)-*O*-(2,4,6-trinitrophenyl) adenosine-5′-triphosphate, an analog of adenosine triphosphate. *Biochim. Biophys. Acta 320*, 635–647.
32. Gill, S., and von Hippel, P. H. (1989) Calculation of protein extinction coefficients from amino acid sequence data. *Anal. Biochem. 182*, 319–326.
33. Brissette, P., Ballou, D. P., and Massey, V. (1989) Determination of the dead time of a stopped-flow fluorometer. *Anal. Biochem. 181*, 234–238.
34. Lakowicz, J. R. (1983) Principles of Fluorescence Spectroscopy, Plenum Press, New York.
35. Fersht, A. (1999) Structure and Mechanism in Protein Science, W. H. Freeman and Co., New York.
36. Johnson, K. A., Simpson, Z. B., and Blom, T. (2009) Global kinetic explorer: A new computer program for dynamic simulation and fitting of kinetic data. *Anal. Biochem. 387*, 20–29.
37. Johnson, K. A., Simpson, Z. B., and Blom, T. (2009) FitSpace explorer: An algorithm to evaluate multidimensional parameter space in fitting kinetic data. *Anal. Biochem. 387*, 30–41.
38. Patel, S. S., Bandwar, R. P., and Levin, M. K. (2003) Transient-state kinetics and computational analysis of transcription initiation. In Kinetic Analysis of Macromolecules (Johnson, K. A., Ed.) pp 87−129, Oxford University Press, Oxford, U.K.
39. Stewart, R. C. (2005) Analysis of ATP binding to CheA containing tryptophan substitutions near the active site. *Biochemistry 44*, 4375–4385.
40. Gutfreund, H. (1995) Kinetics for the life sciences: Receptors, transmitters, and catalysts, Cambridge University Press, Cambridge, U.K.
41. Strickland, S., Palmer, G., and Massey, V. (1975) Determination of dissociation constants and specific rate constants of enzyme-substrate (or protein-ligand) interactions from rapid reaction kinetic data. *J. Biol. Chem. 250*, 4048–4052.
42. Robertson, B. A., Schroeder, G. K., Jin, Z., Johnson, K. A., and Whitman, C. P. (2009) Pre-steady-state kinetic analysis of cis-3-chloroacrylic acid dehalogenase: Analysis and implications. *Biochemistry 48*, 11737–11744.
43. Levin, M. K., Hingorani, M. M., Holmes, R. M., Patel, S. S., and Carson, J. H. (2009) Model-based global analysis of heterogeneous experimental data using gfit. *Methods Mol. Biol. 500*, 335–359.
44. Kuzmic, P., Lorenz, T., and Reinstein, J. (2009) Analysis of residuals from enzyme kinetic and protein folding experiments in the presence of correlated experimental noise. *Anal. Biochem. 395*, 1–7.
45. Hiratsuka, T. (2003) Fluorescent and colored trinitrophenylated analogs of ATP and GTP. *Eur. J. Biochem. 270*, 3479–3485.
46. Oswald, C., Jenewein, S., Smits, S. H. J., Holland, I. B., and Schmitt, L. (2008) Water-mediated protein-fluorophore interactions modulate the affinity of an ABC-ATPase/TNP-ADP complex. *J. Struct. Biol. 162*, 85–93.
47. Berezov, A., Zhang, H. T., Greene, M. I., and Murali, R. (2001) Disabling erbB receptors with rationally designed exocyclic mimetics of antibodies: Structure-function analysis. *J. Med. Chem. 44*, 2565–2574.
48. Goyal, M., Rizzo, M., Schumacher, F., and Wong, C. F. (2009) Beyond thermodynamics: Drug binding kinetics could influence epidermal growth factor signaling. *J. Med. Chem. 52*, 5582–5585.
49. Tummino, P. J., and Copeland, R. A. (2008) Residence time of receptor-ligand complexes and its effect on biological function. *Biochemistry 47*, 5481–5492.
50. Hoops, S., Sahle, S., Gauges, R., Lee, C., Pahle, J., Simus, N., Singhal, M., Xu, L., Mendes, P., and Kummer, U. (2006) COPASI: A COmplex PAthway SImulator. *Bioinformatics 22*, 3067–3074.
51. Kuzmic, P. (1996) Program DYNAFIT for the analysis of enzyme kinetic data: Application to HIV proteinase. *Anal. Biochem. 237*, 260–273.